Analysis of surface deformation and related factors over mining areas based on InSAR: A case study of Fengcheng mine

Xiaying Wang[1,2], Shuaiqiang Chen[1,2], Yuanping Xia[1,2*], Yufen Niu[3], Jun Gong[4], Yumei Yang[1,2]

[1]Key Laboratory of Mine Environmental Monitoring and Improving around Poyang Lake of Ministry of Natural Resources, East China University of Technology, Nanchang 330013, China; 201960018@ecut.edu.cn(X.W.); 2021110348@ecut.edu.cn(S. C.); ypxia@ecut.edu.cn(Y. X.); 2021110158@ecut.edu.cn(Y. Y.)
[2]School of Surveying and Geoinformation Engineering, East China University of Technology, Nanchang 330013, China;
[3]School of Mining and Geomatics Engineering, Hebei University of Engineering, Handan, 056038, China; niuyufen@hebeu.edu.cn (Y.N.)
[4] Geological Environment Monitoring Institute of Jiangxi geological survey and Exploration Institute, Nanchang, 330006, China; m15270916006@163.com(J. G.)

Keywords: InSAR, Time-series Deformation, Fengcheng Mine Area, Correlation Analysis

Abstract

Ground surface deformation in mines affects mining production, damages the ecological environment, and endangers human safety. Mastering the detailed time series deformation and related triggering factors can provide key information for the safety of the mining area. Therefore, the Fengcheng mining area, a large and ancient coal mine in Jiangxi Province, China, was selected as the study area in this work, and the following research was conducted: 1. The accuracy and applicability of the Stacking, Small-Baseline Subset InSAR (SBAS-InSAR), and Interferometric Point Target Analysis (IPTA) methods were preliminarily explored while monitoring the annual deformation rate based on Sentinel-1A data from October 2019 to November 2022. 2. The time-series deformation of the Fengcheng mining area was obtained with SBAS-InSAR technology, and the sedimentation was validated with leveling results. 3. The correlation factors of deformation, such as rainfall and land cover, were studied, and the relationship between the influencing factors, such as coal mining dip angle, digital elevation, coal mining elevation, and deformation, was quantitatively explored with the Grey correlation model and Pearson correlation analysis method. The following conclusions were drawn: The SBAS method has the best adaptability in the dense vegetation mining area, and the root-mean-square error of the difference between deformation results and leveling data does not exceed 4mm. The evolution process of deformation centers is mainly divided into the stages of initial deformation, constant velocity deformation, accelerated deformation, and stable condition. Compared with the natural factors, the settlement of the Fengcheng mining area is mainly affected by human-induced mining and construction of artificial facilities.

1. Introduction

Geological mining disasters refer to the deformation of shallow surface rock and soil bodies due to extraction of large amounts of mineral resources during mining activities, causing serious consequences in the geological and hydrogeological conditions and the natural environment, thus destroying mining engineering equipment and the resource environment of the mining area, affecting the mining production, and endangering the safety of human life and property. Fengcheng City in Jiangxi Province, with a long history of mining coal, kaolin, ceramic clay, and other minerals, is rich in mineral resources and especially coal resources, which are ranked first in the province(Government, 2022a). Historically, geological disasters have occurred many times in Fengcheng City. Three collapses occurred in the Pinghu coal mine in 1996, 2001, and 2003 during the working face mining process and after the cessation of mining, with the deepest cave-in pits as high as 5 m and 20 m in diameter. In March 2014, Fengcheng urban area discovered a large pit with the extent of 1800m^2 and depth of 15 m, which occurred mainly because of coal mining and groundwater extraction and was accompanied by ground subsidence(Hu, 2012). Therefore, surface subsidence caused by underground mining activities is a serious engineering, economic, and environmental problem(Bateson et al., 2015; Ng et al., 2017; Fan et al., 2021). Meanwhile, the mine geohazards can be indirectly reflected by the deformation state of the shallow surface; therefore, the fine monitoring of mine surface deformation provides detailed information for the prevention of mine hazards(Zheng et al., 2018; Wang et al., 2020; Zhou et al., 2020).

Synthetic aperture radar (SAR) interferometry has become an irreplaceable remote sensing technology for Earth observation with the advantages of high accuracy, wide coverage, and all-day and all-weather application(Osmanoglu et al., 2016; Wang et al., 2018; Wang et al., 2023). Firstly, differential interferometric synthetic aperture radar (D-InSAR) laid the foundation for InSAR development(Graham, 1974). However, D-InSAR technology only reflects ground surface changes information between two scenes, and the information is the combination of ground deformation, sensor positioning error, digital elevation model error, atmospheric delay and other factors, which induces great inconvenience for study of the long-term deformation state and extracting accurate deformation values, thus largely restricting the accuracy of true deformation(Liu et al., 2013; Havazli and Wdowinski, 2021). In order to overcome the above drawbacks, a series of time-series InSAR techniques have been proposed, including Stacking-InSAR(Sandwell and Price, 1998), Persistent Scatterer InSAR (PS-InSAR)(Ferretti et al., 1999), Small-Baseline Subset InSAR (SBAS-InSAR)(Berardino et al., 2002), and the subsequent and continuously improved techniques such as

Multi-Temporal InSAR (MT-InSAR) and Temporarily Coherent Point InSAR(Hooper, 2008; Casu et al., 2011; Ferretti et al., 2011; Zhang et al., 2012; De et al., 2017; Amedeo et al., 2023).

The application of InSAR technology in mine ground surface deformation monitoring has been promoted with the continuous development of InSAR. Firstly, the usability of the InSAR technique for coal mine surface subsidence was verified in 1996(Carnec et al., 1996); subsequently, InSAR technology was progressively used to monitor the land subsidence in mining areas(Perski, 1998; Wegmuller et al., 2000; Colesanti et al., 2005; Ge et al., 2007; Jung et al., 2007; Baek et al., 2008; Ng et al., 2011; Bhattacharya et al., 2012; Przyłucka et al., 2015). Then, many researchers(Zhang et al., 2019; Yuan et al., 2021; Wang et al., 2022; Wang, 2022; Xu et al., 2022; Yao et al., 2023) analyzed the kinetic process of mine subsidence, combining the InSAR technology and the characteristics of the mine area. The significance of those research works lies in their study of the evolution process of the mine ground surface with the aim of preventing geological mining disasters. However, for mine areas with a large amount of vegetation and few structures, the accuracy and applicability of various InSAR techniques in obtaining ground surface subsidence and the detailed correlation factors still need to be further explored.

Therefore, this work, taking Fengcheng mine as the study area, explored the applicability of InSAR technologies (Stacking, SBAS, IPTA) in mining areas, obtained the time-series deformation, and quantitatively analyzed the correlation factors of mining subsidence.

2. Research Areas and Data Introduction

2.1 Overview of Research Areas

The study area is located on the west bank of the Ganjiang River in Fengcheng City, Jiangxi Province, and belongs to the key area of the Fengcheng coal mining area (as shown in Figure 1). The terrain and landform are mainly composed of low mountainous areas, hills, and river valley alluvial plains. There are seven coal mines distributed in the area, namely, Shishang, Qujiang, Dongshenling, Yunzhuang, Wusheli, Meixianling, and Xianguling, including medium-sized coal mines such as Shishang pit, Shangzhuang pit, Qujiang pit, Jianxin Mine, and Pinghu Mine, as well as 27 small-sized coal mines, such as Shangfeng Coal Mine, Dongshenling Coal Mine, Kengtang Coal Mine, Majiang Coal Mine, and Hongda Coal Mine. To remediate the mining environment, some of the mines in the study area have ceased mining for more than five years, for example, Yunzhuang Coal Mine, Pinghu Coal Mine, and Jianxin Coal Mine. The only mines currently in operation are the Shangzhuang Coal Mine and the Qujiang Coal Mine(Government, 2020; Government, 2022b).

The main coal seams mined in the study area are the B and C coal seams of the Permian Upper Leping Formation, Permian Upper Longtan Formation, and Triassic Upper Anyuan Formation. The Anyuan Formation is only locally developed in the mining area, and the main coal seam of the Permian Upper Longtan Formation B4 is in the Laoshan section of the group, with stable seams developed in the whole area. Coal group C is located in the Wangpanli section of the group, with many coal seams and a large area containing coal, but the thickness of a single seam is small, the dip angle is 5~32°, the thickness of mined seam is 0.60~4.22m, the elevation of mined seam is +80~-1300m, and the elevation of most of the areas in this region is 30~50m. The coal mining method is generally wall or strip mining, and the full collapsing method is utilized for roof management. For roof support, a miscellaneous wood frame box support or I-steel support is adopted, while for some, the joint slurry spraying active support with the anchor ladder beam and the full-section hanging net are used. The lithology of the coal seam roof in the area is mainly siltstone, fine sandstone, and mudstone and is categorized as an easily caving to medium caving roof.

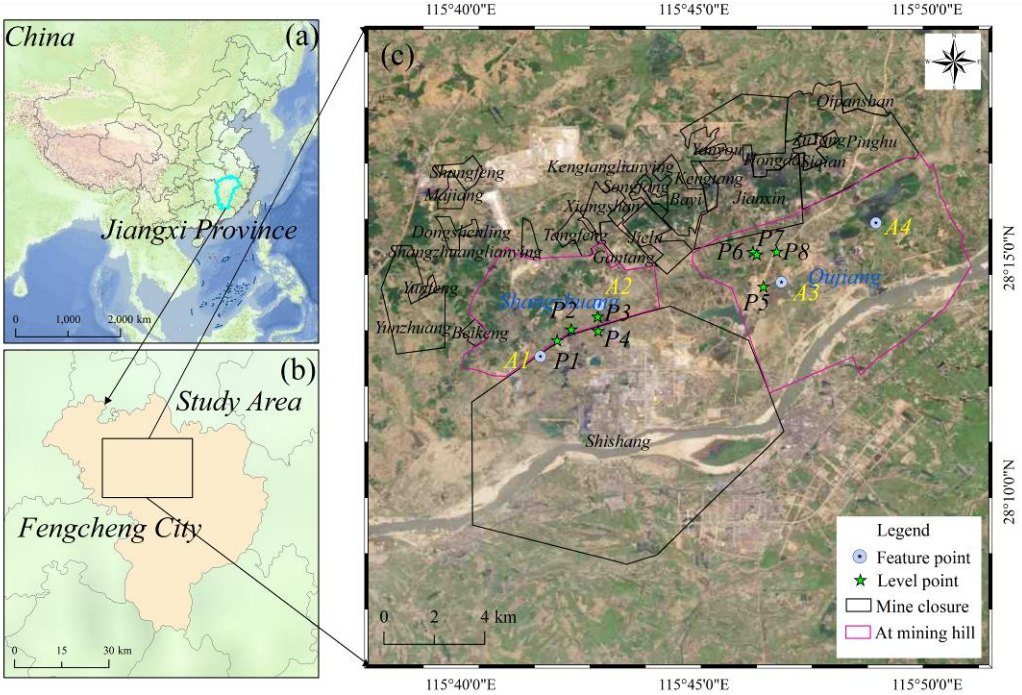

Figure 1. Geographic distribution of coal mines in Fengcheng City (a, b) and distribution of closed coal mines, coal mines in operation, level points, and feature points in the Fengcheng mining area (c).

2.2 Introduction of Data Sets

2.2.1 SAR Data Sets: In this study, 91 Sentinel-1A ascending orbit images were collected from 30 October 2019 to 7 November 2022 with polarization mode VV+VH, Path 40, Frame 87, and an image interval of 12 days. The specific parameters are shown in Table 1.

2.2.2 Other Data Sets: The precision orbit data were downloaded from the official website of the European Space Agency (https://scihub.copernicus.eu/gnss/#/home); the digital elevation model (DEM) was generated by the Shuttle Radar Topography Mission (SRTM) in 2000 with a resolution of 30m. The building height estimation model with 10 m resolution (CNBH-10m) was constructed by Dr Wu using multi-source Earth observation data and machine learning techniques(Wu et al., 2023). Land use data were extracted from a global LULC map with 10 m resolution for the years 2019–2021 which was created by Karra with Sentinel-2 data(Karra et al., 2021). Other data related to mining were obtained from field measurements.

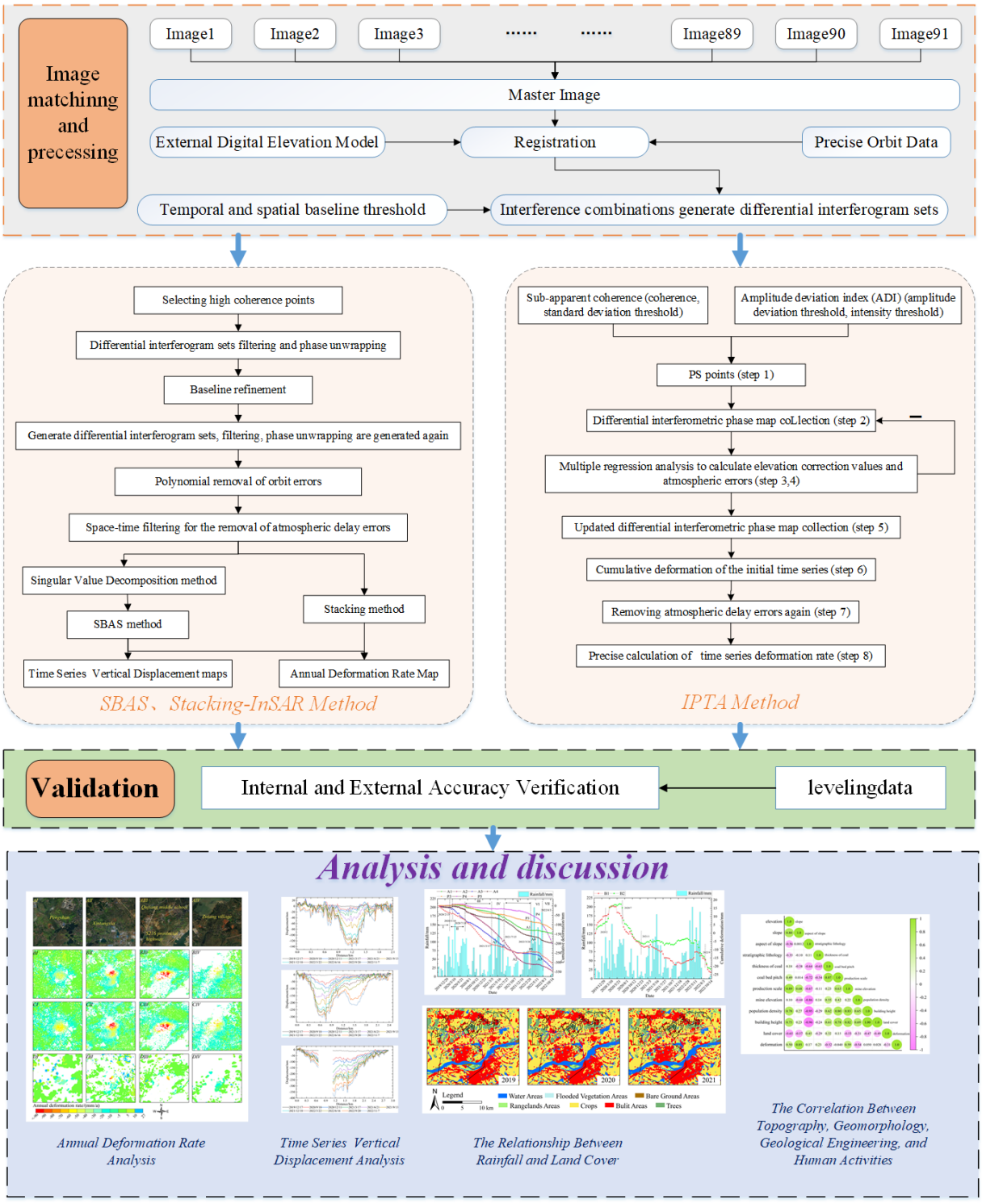

Figure 2. Technical roadmap of this study.

2.2.3 Related Software: We used the GAMMA synthetic aperture radar interferometry software produced by the Swiss company GAMMA Remote Sensing AG as the experimental platform for this work. The final maps were displayed using ArcGIS software.

Table 1. The description of data parameters.

Satellite Sensor	Parameter	Value
Sentinel -1A	Central Incidence	33.94°
	Polarization Mode	VV
	Wavelength	5.6cm
	Orbital Direction	Ascending
	Azimuth/Rang Pixel Spacing	13.96/2.33m
	Number of Images; Acquisition Time	91; 2019-10-30~2022-11-07

3. Research Methods and Process

The mine subsidence was acquired using three kinds of InSAR tech-niques, namely, Stacking, SBAS, and IPTA. Meanwhile, Pearson correlation analysis and the Grey correlation model were used to study the factor corre-lation of the mine subsidence results.
The technical route of our research is shown in Figure 2.

3.1 Generation of Displacement with InSAR Technology

In this study, data pre-processing was conducted in the following steps. Firstly, 91 SAR images covering the study area were obtained, and speckle noise reduction with a multi-look ratio of 4:1 in range and azimuth directions was carried out, followed by converting the DEM from the geographic frame to the radar Doppler coordinate system and conducting SAR image registration. Secondly, due to year-round lush vegetation and summer rains in the research area, we constructed 292 interferograms within the spatial and temporal thresholds of 50 days and 100 m. Then, adaptive filtering was employed to eliminate random noise, and the minimal cost flow was used for unwrapping the interferometric phase. Finally, after removing the flat Earth effect and terrain phase influence with external DEM data, the phase information in the jth differential interferogram is expressed as follows (Equation 1):

$$\Delta\varphi_j = \varphi_{def} + \varphi_{topo} + \varphi_{atm} + \varphi_{orb} + \varphi_{noise} \quad (1)$$

Where φ_{def} is the deformation phase, φ_{topo} the residual terrain phase introduced by DEM errors, φ_{atm} the atmospheric delay phase, φ_{orb} the orbital error phase, and φ_{noise} represents noise phase.
Various InSAR techniques can be applied to obtain time-series deformation and annual mean rate based on the multiple interferometric phase $\Delta\varphi$.

3.1.1 Stacking-InSAR Principle: Assuming that the atmospheric noise in each image is random, the interferogram Stacking technique(Sandwell and Price, 1998) calculates the annual mean deformation rate by superimposing the multiple interferograms. This technique effectively decreases the problem of temporal and spatial incoherence, reduces the effect of atmospheric disturbances, and can improve the accuracy of deformation resolution (Equation 2).

$$v = \sum_{j=1}^{N} \Delta\varphi_j \cdot \Delta t_j \Big/ \sum_{j=1}^{N} \Delta t_j \quad (2)$$

Here, N is the interferogram number, v is the annual rate, and Δt_j is the revisit period; this is also the case in the following sections.

3.1.2 SBAS-InSAR Principle: The SBAS method(Berardino et al., 2002) reduces the impact of incoherence on the quality of interferograms by selecting high-quality pixels in interferograms for the calibration and unwrapping process based on the coherence coefficients. The deformation phase is expressed by the deformation rate with the assumption that the deformation process follows a linear law (Equation 3). While considering the DEM topographic error, the functional equation can be formed for M interferograms (Equation 4).

$$\Delta\varphi_j = \sum_{k=IS_j+1}^{IE_j} \left(t_k - t_{k-1}\right) \cdot v_k,\ j = 1, \cdots, M \quad (3)$$

Here, IE_j and IS_j denote the acquisition time of reference and secondary images.

$$B \bullet v + C \bullet \varepsilon = \Delta\varphi \quad (4)$$

Here, B is an $M \times N$ dimensional matrix. For each element of row j, $B(j,k) = t_k - t_{k-1}$, and the rest are zero. C is an $M \times 1$ matrix, and the DEM error is ε.
If the N images form L subsets, then $B = N - L + 1$, and Equation (4) will have an infinite number of solutions, so the least squares solution at the minimum number of paradigms is obtained using the Singular Value Decomposition (SVD) method. The atmospheric delay phase and nonlinear deformation phase are extracted by filtering the residual phase in both time and space domains. Thus, the SBAS-InSAR technique removes atmospheric delay error from the above interferometric pairs of multi-master images and then uses the SVD method to calculate the deformation rate in each period to obtain the long-term land surface deformation.

3.1.3 IPTA Principle and Process: The Interferometric Point Target Analysis (IPTA) technique(Werner et al., 2003) mainly analyzes the temporal deformation of scattering points, which are selected according to coherence, standard deviation threshold, amplitude deviation threshold, and intensity threshold. These points are mostly strong scattering features such as buildings, concrete embankments, rocks, railway tracks, street lamps, or man-made corner reflectors. IPTA is usually used for monitoring urban areas, and the steps are as follows: 1) identifying PS points based on sub-visual coherence values (coherence, standard deviation threshold) and amplitude deviation threshold (amplitude deviation threshold, intensity threshold); 2) calculating the differential interferometric phase and the corresponding elevation value for each PS point; 3) conducting spatial or temporal dimensional phase unwrapping to calculate the atmospheric delayed phase associated with the elevation; 4) computing elevation corrections and residual

phases via multiple regression analyses and conducting spatial domain filtering to isolate long-wavelength atmospheric phases in the residual phases; 5) removing the elevation correction value and the atmospheric delay phase from the original differential interferometric phase; 6) initially calculating the time-series deformation and converting the multi-master image to a single-master image and removing atmospheric delay phase from the single-master image time series again (mask deformation area, spatial domain filtering, removal of atmospheric phase); 7) calculating the deformation rate of the time series: the cumulative deformation phase is converted to a cumulative deformation value, and the deformation rate is recalculated based on the cumulative phase of the time series.

In this study, based on multi-master images and single-look interferograms, we firstly set a coherence threshold of 0.3, standard deviation threshold of 0.7, amplitude deviation index threshold of 1.1, and intensity threshold of 0.15 and obtained 2561428 candidate points. Then, the elevation error and atmospheric delay error were calculated with repeated iterative regression analysis. At the same time, we further screened PS points and only retained stable PS points. Finally, the average annual rate of PS points was calculated, and the line-of-sight deformation was converted to vertical deformation values by taking into account the subsidence characteristics of the study area.

3.2 Correlation Analysis Methods

The occurrence of ground deformation is the result of the combined effect of multiple internal and external dynamic factors, and the selection of its influencing factors is critical to the study's results. The conventional influencing factors are topography, stratigraphy, lithology, and so on, but the explanatory strength of the universal factors for the surface deformation of the mining area is limited. As a result, after thorough examination of the various influencing factors of the Fengcheng coal mine, we further introduced the mining data as the correlation factors, including elevation, slope, aspect of slope, stratigraphic lithology, the thickness of coal, coal bed pitch, production scale per unit area, mine elevation, population density, building height, and land cover type.

To unify the resolution of all the influencing factors, we resampled the raster pixel size of all the influencing factors to that of the deformation rate. Due to the meaning represented by the values in each influence factor differing, the data were normalized to ensure that the scale variation between variables did not have a major impact on the analysis results. Finally, the Grey correlation model and Pearson correlation analysis were utilized to calculate the link between each factor and deformation.

3.2.1 Pearson Correlation Analysis: Pearson correlation analysis (Benesty et al., 2009) is used to quantitatively study the relationship between data, and the correlation strength can be reflected in the correlation coefficient r, which ranges from -1 to 1. A larger absolute value of the coefficient means a greater degree of correlation; that is, a coefficient $|r|$ close to 1 indicates completely related and vice versa. The formula for the correlation coefficient is as follows (Equation 5):

$$r = \frac{\sum (x_i - m_x)(y_i - m_y)}{\sqrt{\sum (x_i - m_x)^2 \sum (y_i - m_y)^2}} \tag{5}$$

where m_x and m_y are the mean values of x and y, respectively.

3.2.2 Grey Correlation Model and Process: The basic principle of the Grey correlation model is to measure the strength of a parameter influenced by other factors. The correlation degree between factors is mainly described by the correlation magnitude(Fu et al., 2013). The correlation coefficient ζ in the Grey correlation model is displayed in Equation (6).

$$\zeta_i(k) = \frac{\min\limits_i \min\limits_k |x_0(k) - x_i(k)| + \rho \max\limits_i \max\limits_k |x_0(k) - x_i(k)|}{|x_0(k) - x_i(k)| + \rho \max\limits_i \max\limits_k |x_0(k) - x_i(k)|} \tag{6}$$

Here, $x_0(k)$ is the parent series, that is, the shape variable in this research, and $x_i(k)$ is the sub-sequence, that is, the shape of the various factors affecting the variable, where ρ is the discrimination coefficient, $\rho > 0$, which usually takes a value of 0.5.

Arranging the correlation degree between sub-sequences and the same parent sequence in order of magnitude will form a correlation sequence r_i (Equation 7).

$$r_i = \frac{1}{n}\zeta_i(k), k = 1, 2 \cdots, n \tag{7}$$

4. Results and Validation

This section demonstrates the deformation annual rate and time-series results of the Fengcheng mining area, and verification results.

4.1 Results

4.1.1 Annual Deformation Rate: The surface deformation results of the Fengcheng mine area from October 2019 to November 2022 (Figure 3) were obtained by performing Stacking, SBAS, and IPTA with 91 Sentinel-1A images.

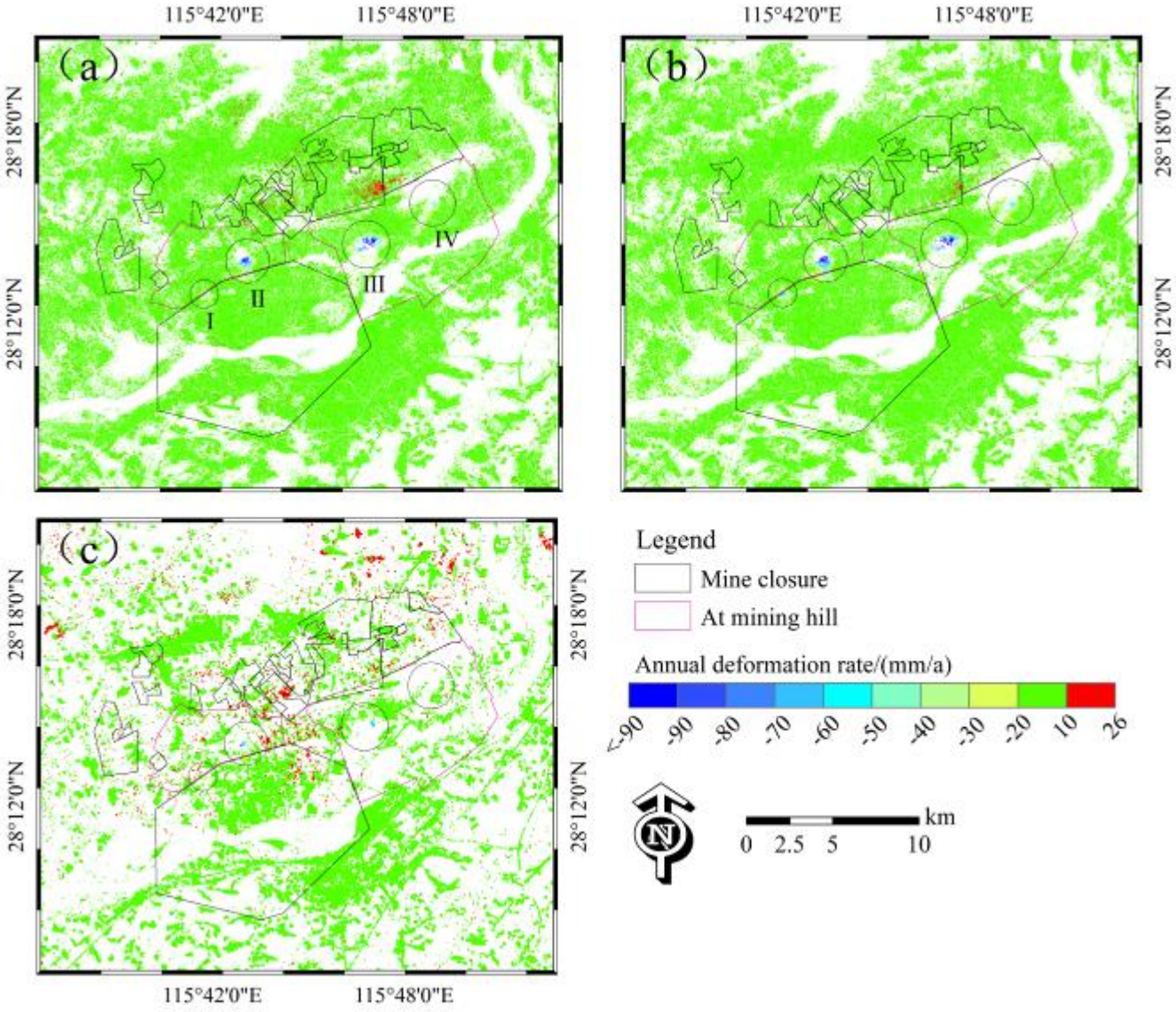

Figure 3. The average deformation rate of the Fengcheng mining region: (a) the annual deformation rate determined by Stacking technology, (b) SBAS technology, and (c) IPTA technology. The purple shape marks the scope of the mining area currently being mined, while the mining areas labeled with black polygons have been closed.

4.1.2 Time-series Deformation: The time-series deformation map (Figure 4) of the Fengcheng mine area between October 30, 2019, and November 7, 2022, created with the SBAS-InSAR technique, shows four subsidence funnels (I, II, III, and IV) in the Shangzhuang and Qujiang coal mines.

4.1.3 Influence Factor Correlation: The correlation coefficients between each influencing factor were calculated and plotted using Pearson correlation analysis (Figure 5). According to the Grey correlation model, these influence factors are listed from strong to weak in order of correlation: production scale per unit area (0.82), building height (0.75), stratigraphic lithology (0.73), population density (0.72), slope (0.71), elevation (0.70), mine elevation (0.66), land cover type (0.65), coal bed pitch (0.65), coal thickness (0.61), and aspect of slope (0.56). The evaluation factor with the highest correlation is production scale per unit area, and the evaluation factor with the lowest correlation is the slope direction, in which the correlation between the land cover type and coal bed pitch is equal.

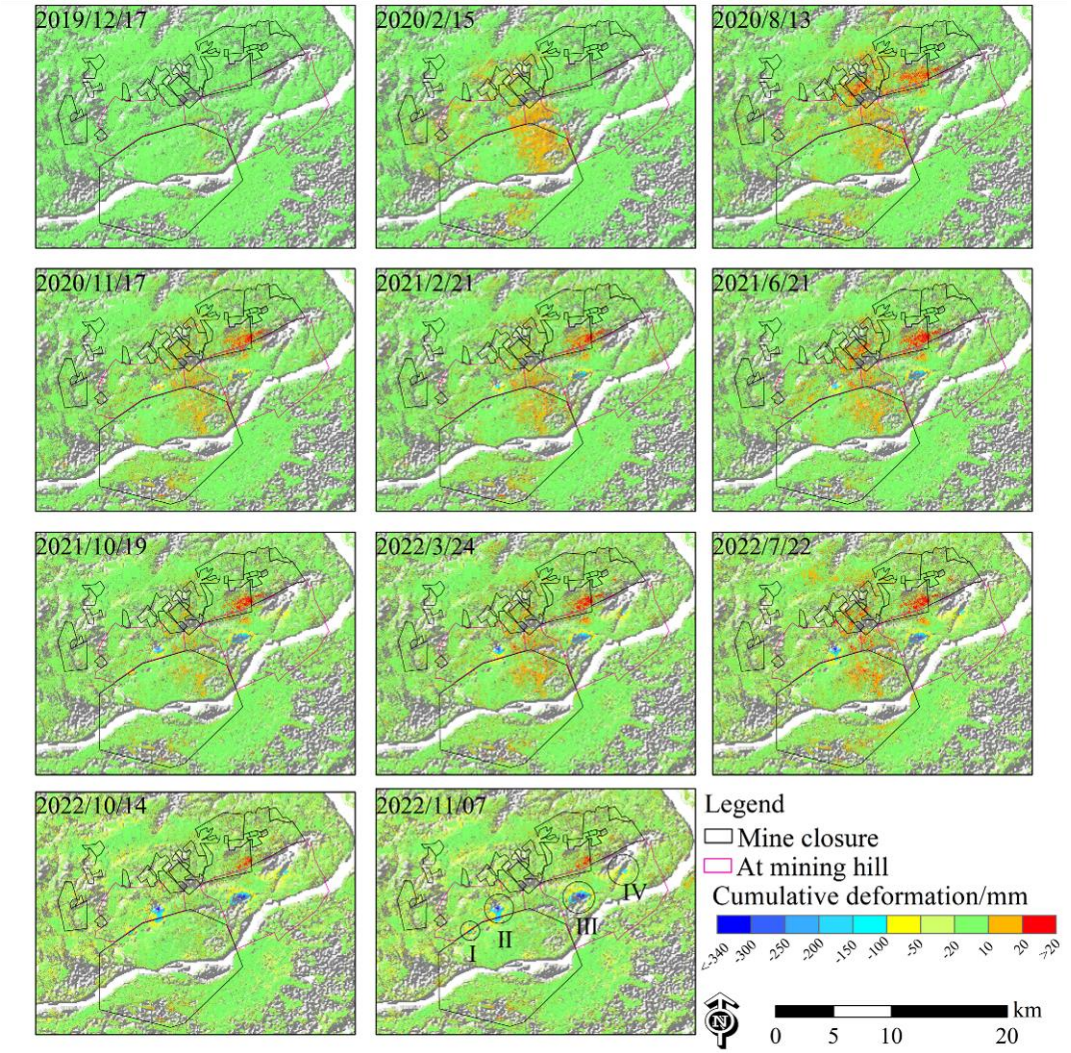

Figure 4. The time-series deformation map of the Fengcheng mining area during October 30, 2019, and November 7, 2022.

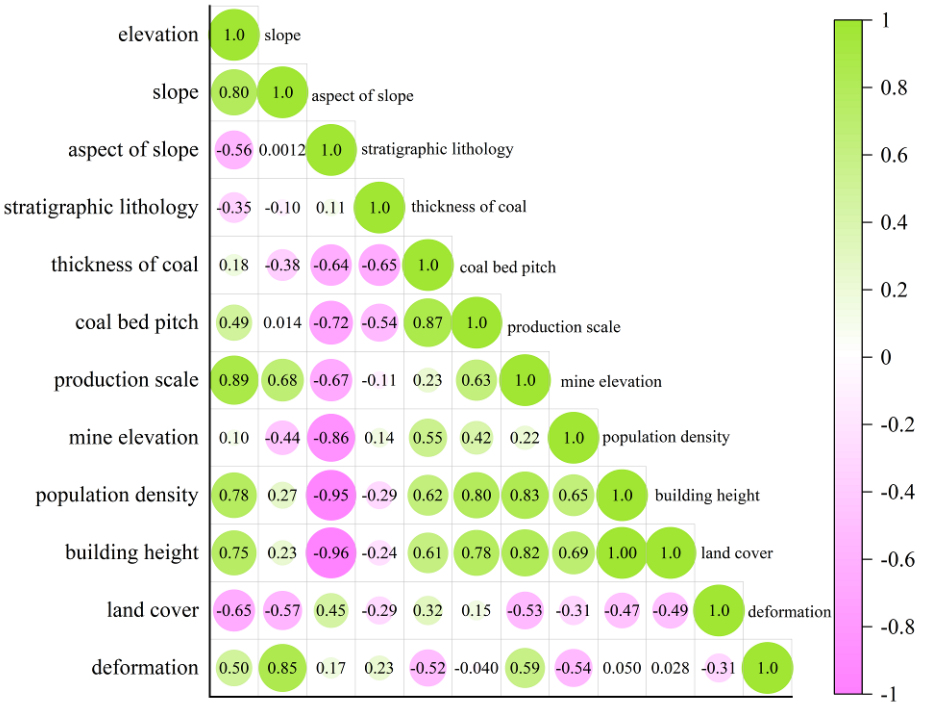

Figure 5. Pearson correlation coefficient diagram between various influencing factors.

4.2 Validation

This section explores the accuracy of deformation results from two perspectives: one is a comparison between different technologies, and the other is a comparison of the deformation using InSAR with the leveling data.

4.2.1 Annual Average Rates from Different Techniques: Since the deformation rate result of the IPTA method has too few PS points located in the mining area, the difference in the annual deformation rates between the IPTA results and the other two methods will not be discussed in this section.

To unify the spatial position of SBAS and Stacking results, we interpolated the null values with the distance weight approach and obtained the difference between the Stacking and SBAS deformation. The statistical histogram is depicted in Figure 6(a). The distribution interval of the difference is within [-10, 5] mm, and the mean and standard deviation are 2.68 and -3.31 mm, respectively, which are, in general, consistent with the normal distribution.

To further investigate the relationship between the results obtained using SBAS and Stacking, the mean annual deformation rates of the same name points obtained with the two techniques were compared, and a scatter plot was generated by using the mean annual deformation rate of the SBAS points as the horizontal axis and that of the Stacking points as the vertical axis (Figure 6b). Pearson's correlation analysis yielded a correlation coefficient r of 0.9339, indicating that the results of the two mean annual deformation rates are extremely consistent.

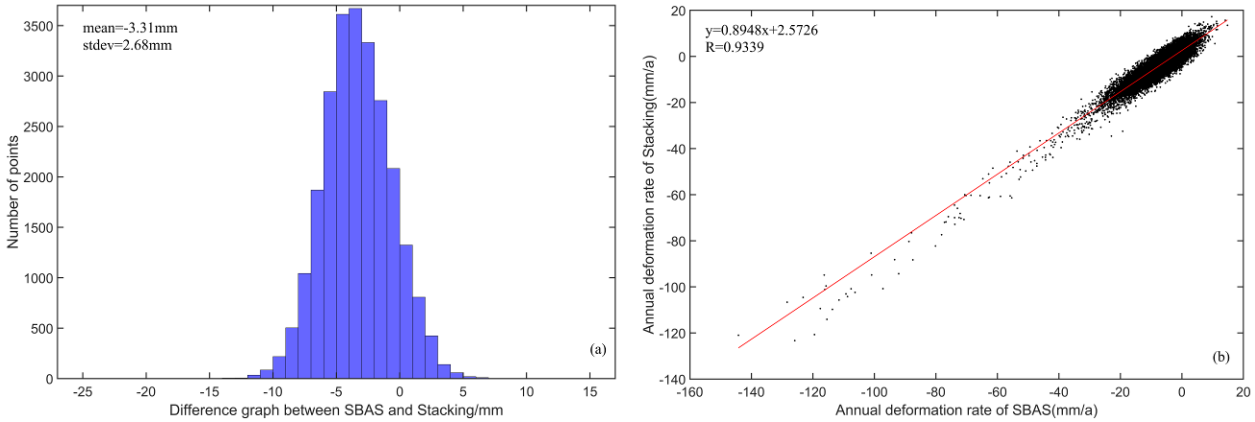

Figure 6. Comparison between SBAS and Stacking results: (a) statistical histogram of the difference in deformation rates between SBAS and Stacking; (b) correlation between the deformation rate of SBAS and stacking.

4.2.2 Comparison of Annual Average Rate Results Using Leveling Data: We compared the annual deformation rates obtained by using Stacking, SBAS, and IPTA with the corresponding leveling data（see Figure 2 for the locations of the leveling data）, the results are shown in Figure 7. Except for several missing data at some points (1, 2, 5, and 6) with the IPTA method, the results of the three InSAR approaches are consistent with the level data in terms of the deformation trend.

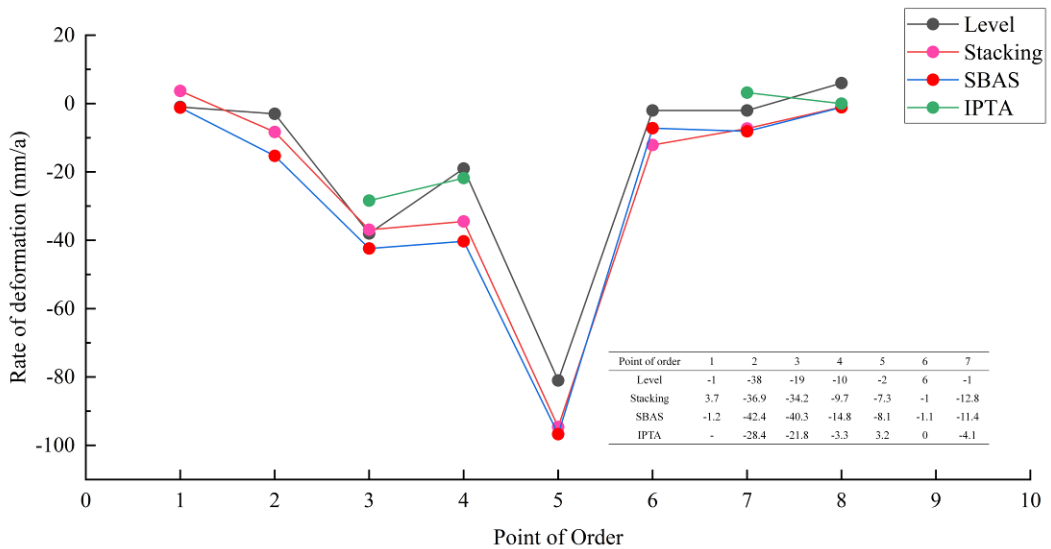

Point of order	1	2	3	4	5	6	7
Level	-1	-38	-19	-10	-2	6	-1
Stacking	3.7	-36.9	-34.2	-9.7	-7.3	-1	-12.8
SBAS	-1.2	-42.4	-40.3	-14.8	-8.1	-1.1	-11.4
IPTA	-	-28.4	-21.8	-3.3	3.2	0	-4.1

Figure 7. Deformation rates of stacking, SBAS, IPTA, and leveling results. The detailed values are shown in the bottom right corner table.

4.2.3 Leveling and Time-series Deformation Results Comparison: This section assesses the dependability of the time-series deformation of the SBAS technique with leveling data. Figure 8 demonstrates that the mean absolute error (MAE)

https://doi.org/10.5194/isprs-archives-XLVIII-1-2024-697-2024

of difference is less than 5mm, and the root-mean-square error (RMSE) is less than 2 mm for seven points. For the point marked P5, InSAR results are lower than those of the leveling monitoring data, which may be due to the InSAR math model not fitting with the deformation process. However, the deformation trend, which can be observed as a simultaneous increase or reduction, is essentially the same for both leveling data and InSAR technology. Generally, there is a high degree of consistency between the leveling monitoring data and InSAR results.

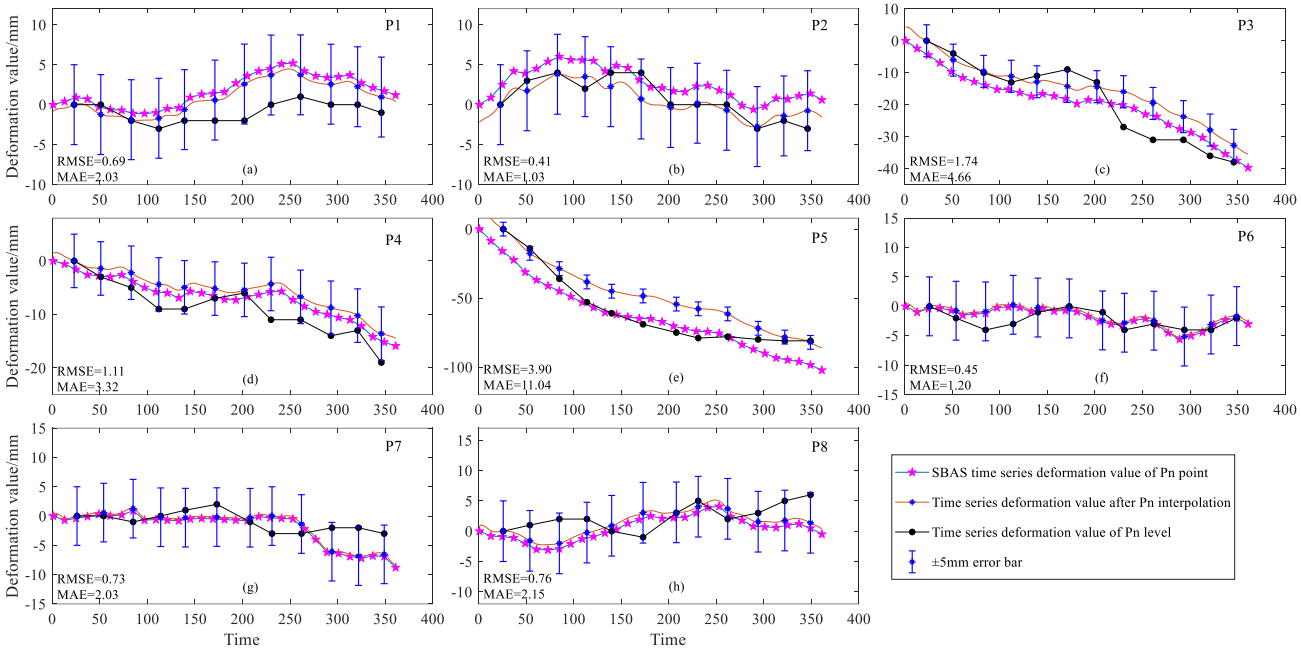

Figure 8. Distribution of SBAS-InSAR and leveling time-series deformation results. The small graphs labeled (a)~(h) represent the time-series deformations at points P1~P8, respectively, and the RMSE and MAE in the lower left corner are the statistical significance values of the results.

5. Analysis and Discussion

We analyzed the deformation evolution process of displacement funnels from the perspective of annual deformation velocity and time-series deformation results, and the correlation factors from the perspective of rainfall, ground surface cover, and the correlated factors.

5.1 Analysis of Deformation Results

5.1.1 Annual Average Deformation Rate: Figure 3 shows the existence of four obvious subsidence areas (I, II, III, IV) in the Shangzhuang and Qujiang coal mines under development which are distributed as funnels. With this and the related high-resolution optical remote sensing picture (Figure 9), the geological location of subsidence areas can be determined. Area I is located on the Pengshan with a maximum annual sedimentation rate of 61 mm/a. Area II is next to the Huojuzhong road and the Xintangxia and surrounded by industrial parks, with an annual rate of deformation of up to -143 mm/a. Region III, close to the S216 provincial highway and Qujiang Middle School, shows a maximum sinking rate of 131 mm/a. Area IV is in the village of Zutang and has a maximum settlement rate of 72 mm/a. Combining the optical image distribution with the null values of the four subsidence regions, we discovered that the large portion of the water body is the main cause of missing data, and the dense vegetation in regions II and III also introduces low coherence.

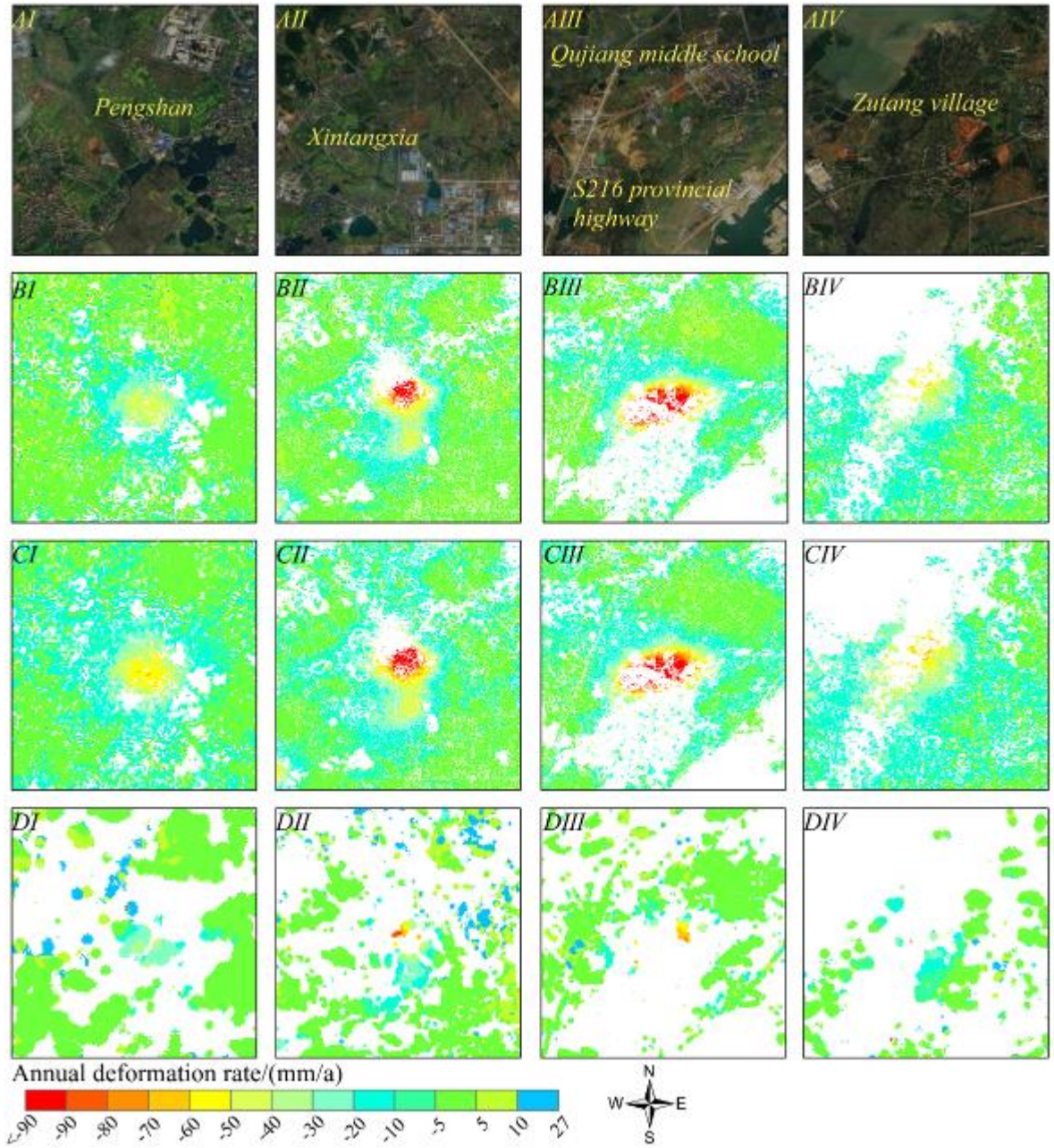

Figure 9. Four sedimentation funnels and corresponding optical images. The first row marked A represents the optical image, the second row marked B is the outcome of the stacking method, C is SBAS, and D is IPTA. The four columns represent four deformation funnels, marked by I, II, III, and IV.

5.1.2 Time-series Deformation: The time-series deformation throughout the monitoring period in Figure 4 displays that the Qujiang and Shangzhuang coal mines progressed steadily, both the cumulative settlement amount and the settlement range increasingly expanded, and the settlement location essentially stayed the same.

From the perspective of displacement centers, the settlement amount and settlement range of Area I continue to grow with the highest cumulative settlement amount of 151mm. In region II, local subsidence occurs on April 15, 2020, and the maximum deformation of the subsidence center reaches 356mm. The greatest quantity of deformation at the center of subsidence in region III is 390mm. The range of deformation is steadily growing, and the magnitude of the deformation increases as time moves on. The settlement center in Area IV has a maximum deformation value of 210mm. To further analyze the evolution process and the deformation distribution of the ground surface, we selected three profiles AA', BB', and CC' in areas I, II, and III and plotted the time-series deformation maps (the locations of the profiles are shown in Figure 10).

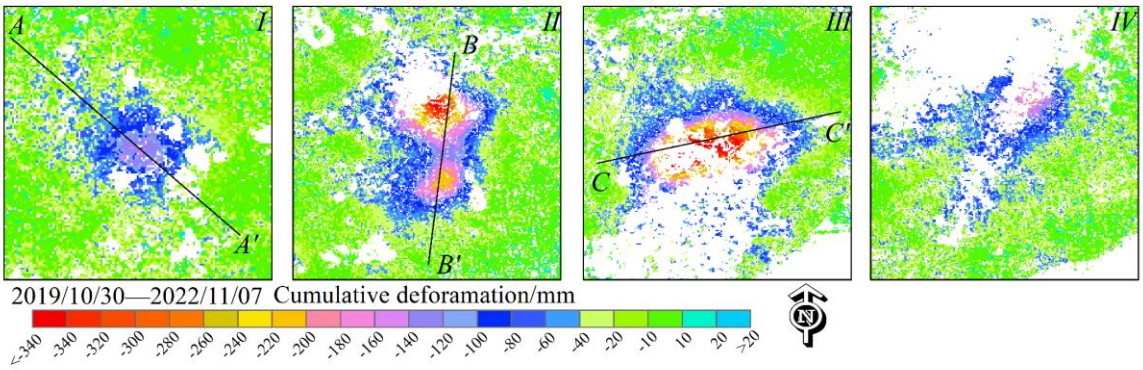

Figure 10. The four accumulative deformation centers and the distribution of corresponding profiles (AA', BB', and CC').

Figure 11(a) displays the time-series deformation of profile line AA' traversing subsidence area I. The profile maximum settlement value reaches 141.6mm during December 2019 and November 2022, and the fastest deformation occurs between March and December in 2021. According to the time-series deformation of the subsidence center, the maximum subsidence is 16.2mm from December 2019 to September 2020, and then the subsidence rate increases slowly. However, the deformation suddenly intensifies from September to December 2021, leading to a three-month subsidence difference of 34.3mm. The rate of deformation gradually decreases, and the difference of subsidence from September to November 2022 is only 2.1mm, indicating that stability is reached. Generally speaking, the beginning subsidence rate of the subsidence area I is small, but it progressively increases and approaches the maximum deformation rate before starting to slow down and eventually tending to stabilize.

The time-series fluctuation along profile BB' throughout region II (Figure 11(b)) illustrates two subsidence funnels distributed in the north–south direction. The upper (north) funnel, with a cumulative settlement of up to 331 mm, initially undergoes an acceleration phase from December 2019 to September 2020. Subsequently, the acceleration phase continues until the accelerated settlement values become slow in the beginning of 2022. It is assumed that the stresses on the rock movement caused by the mining operations of the associated mine have reached a new equilibrium. In contrast, the lower subsidence funnel begins to settle at a steady rate of roughly 10 mm every three months from December 2019 to December 2021. After that, the rate of subsidence increases from December 2021 to September 2022; nevertheless, it decreases in magnitude to a maximum settlement of 217.9 mm between September 2022 and November 2022, indicating the ongoing sinking effects of coal mining on the ground.

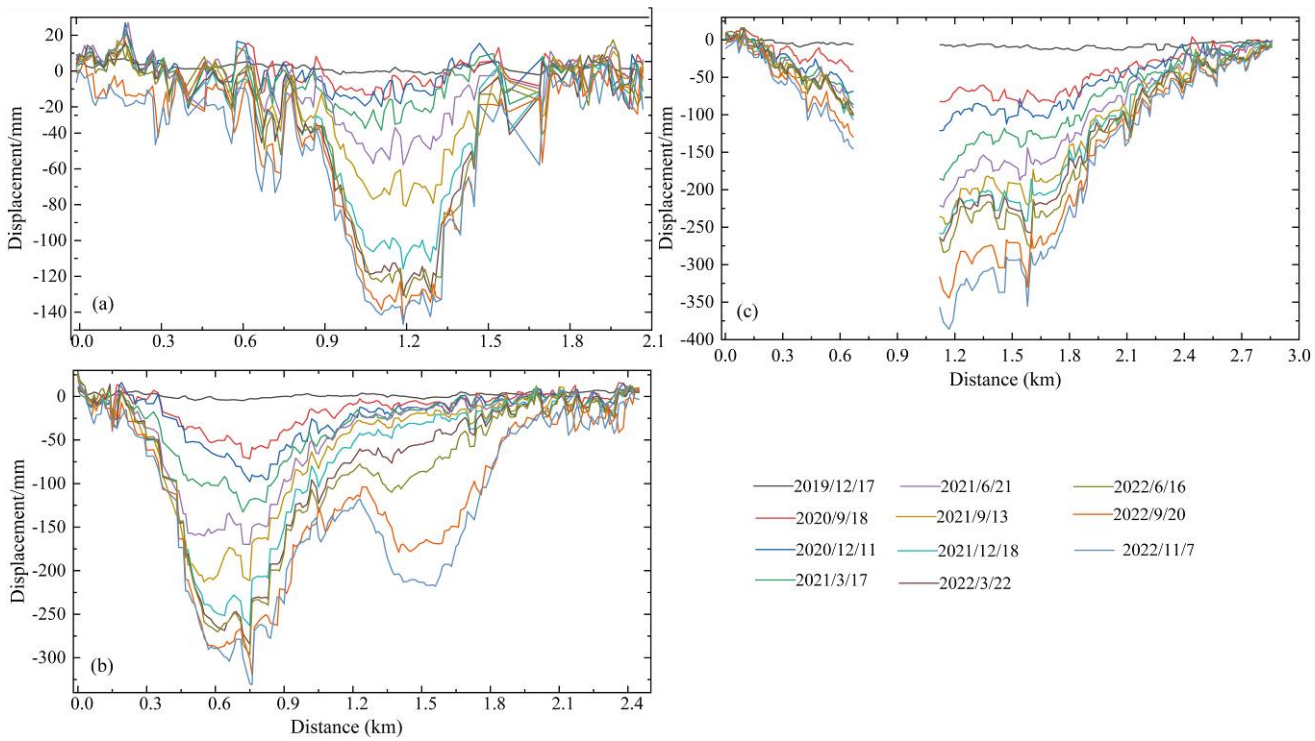

Figure 11. The three charts demonstrate time-series displacement along profile AA' (a), BB' (b), CC' (c) in settlement area I, II and III respectively.

Figure 11(c) displays the time-series displacement of central profile CC' across region III. The missing part from the left side of the subsidence funnel causes the deformation results to be discontinuous in time and space. The highest settlement of

386.2 mm and the very steady settlement rate imply that mining operations were ongoing over the research period.

5.2 Analysis of Correlation Factors

5.2.1 Rainfall: Six characteristic deformation points in the study area were obtained to examine the relationship between rainfall and ground deformation, including the level data points P3, P4, P5, and center of the four sedimentation funnels A1–A4 (the distribution is shown in Figure 2). The cumulative deformation versus rainfall maps of the feature points were produced, and the total rainfall information between the data of each scene was counted (Figure 12).

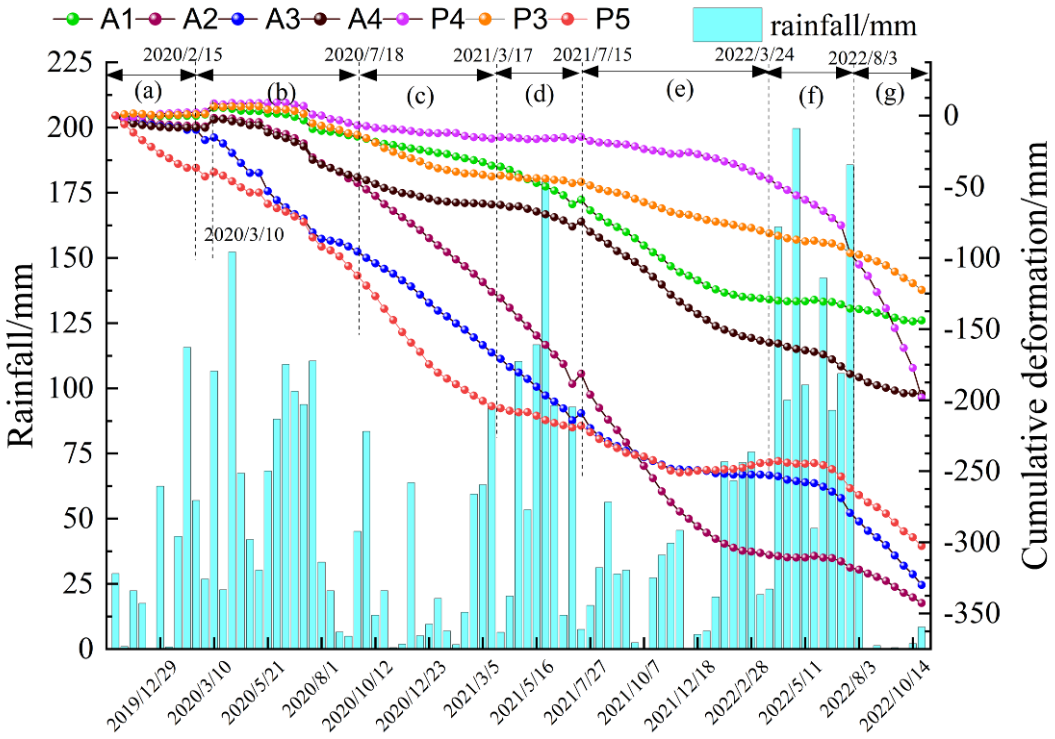

Figure 12. Rainfall and deformation map of feature points, including P3~P5 and A1~A4.

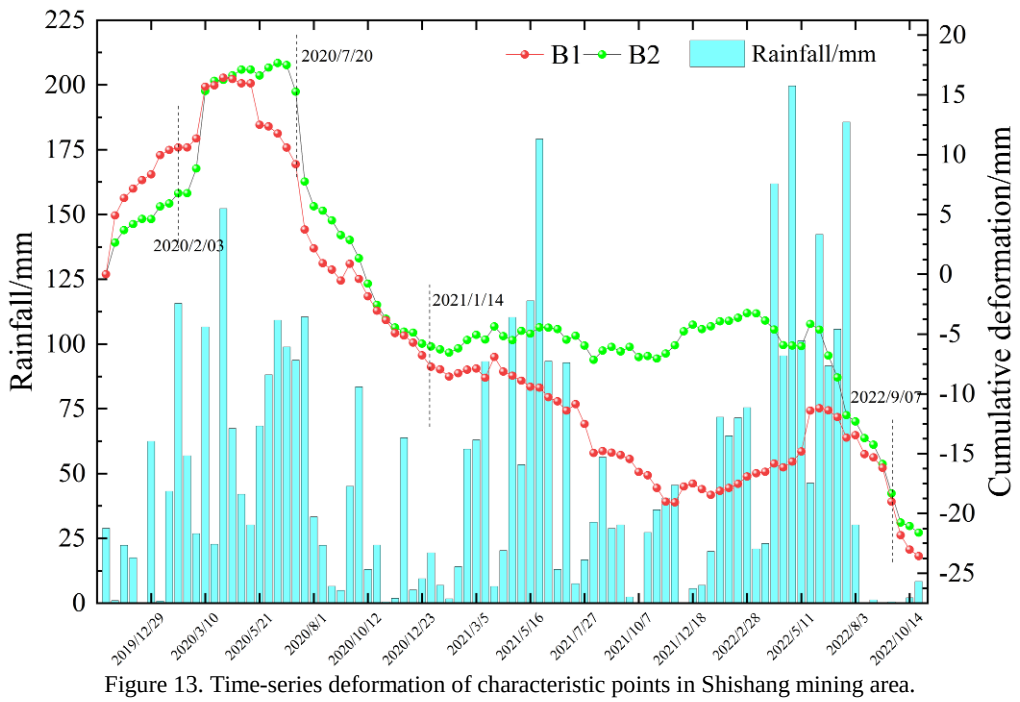

Figure 13. Time-series deformation of characteristic points in Shishang mining area.

Due to the geographical distribution of the six distinct feature sites, the sedimentation time series of each point in Figure 12 demonstrates a different and nonlinear decline and differs in terms of cumulative sedimentation amounts. In response to the analysis of the features of the point deformation trend, the whole study period was divided into seven parts (marked (a)~(g) in Figure 12). In period (a), the deformation of A1, P3, and P4 shows the same magnitude with an interval of [-2.4, 1.54] mm

from September 30, 2019 to February 15, 2020. Then, the deformation curves of A2, A3, and A4 demonstrate a small rise and continue to settle. The point P5, with a deformation value of -36.66 mm by February 15, significantly subsides from the beginning. In period (b) during 10 March and 18 July 2020, there is a weak uplift at points A1, P3, and P4 relative to the original deformation, points A2 and A4 exhibit sedimentation quickly, point A3 begins to settle rapidly, and the settlement values are nearly identical to those of point P5 on July 18. Points P3, A4, and P5 sink quickly, probably due to the rainfall from 18 July 2020 to 17 March 2021.

Generally, during the periods marked (a), (c), (e), and (g), there is less rainfall. However, the rainfall is abundant during (b), (d), and (f). The deformation value of point P5 is most obviously affected by rainfall, following points A1, A4, and P3. The deformation value of point A2 changes significantly with the rainy season. The deformation value of point A3 changes significantly in areas (d), (e), and (f). The initial change in point P4 is the slowest of all points, and it accelerates the sedimentation after June 28, 2022.

To further explore the relationship between rainfall and deformation, we selected two surface feature points (B1 and B2) at the Shishang coal mine (see Figure 15) and plotted the time-series deformation diagram (Figure 13). There is an obvious relationship between cumulative deformation and rainfall, while the deformation value decreases when the rainfall increases and vice versa.

5.2.2 Ground Surface Cover: The land cover type is mainly crop and built-up area within the mining area during the period of 2019-2021 (Figure 14). The extent of the built-up area in different coal mining areas is expanded from 2019 to 2020, and the Shishang coal mine is the most notable. Meanwhile, the distribution of building area and deformation area has a certain consistency. From 2020 to 2021, the growth rate of the built-up area slowed down, with a total increase of 5.94 km^2. The deformation areas, Jielu, Jianxin, and Pinghu coal mines, are mainly located on the new constructions.

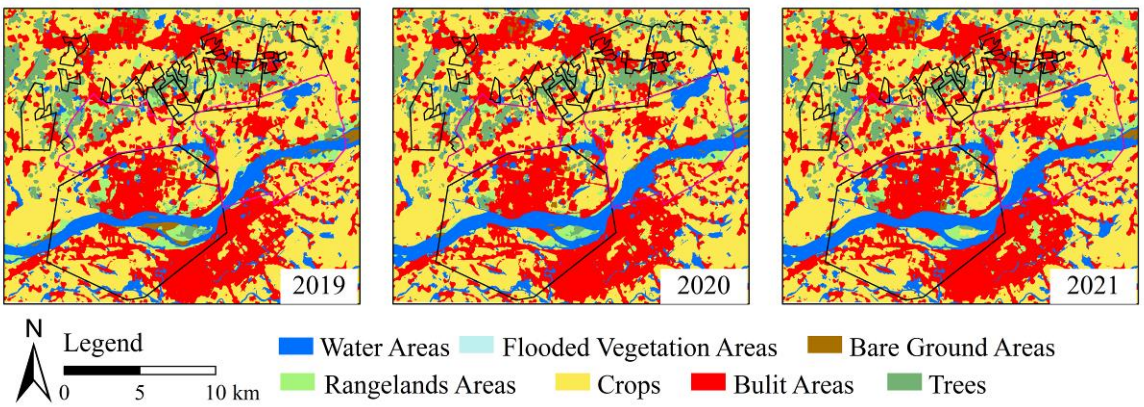

Figure 14. Annual land use type. The three pictures are the land use classification maps for 2020, 2021, and 2022(Karra et al., 2021).

As for the settlement in the Shishang mine area, the reason for this may be that the buildings in the Shishang mine area are already completed, and there is a transition from the ground uplifting to slight ground settlement due to building loads(Government, 2020; Government, 2022b). Combined with historical optical images (Figure 15) with time-series deformation, most of the deformations were uplifted before the buildings were built, and the uplifted deformations weakened or disappeared after the buildings were finished.

Figure 15. Historical images of the Shishang mining area in July 2018, February 2020, July 2020, January 2021, and September 2022. The location of the mining area is shown in Figure 2. The red rectangles indicate areas of building additions.

Combining this with the historical image map and the rainfall results (Figure 13), it can be seen that the building at point B1 was built in July 2020, and after the building was repaired, the deformation value of the point began to decrease, and then the deformation changed from the original lifting to sinking under the influence of the foundation load. There were traces of overturned soil in July 2020 at point B2, and the newly repaired building could be seen on the optical map in September 2022, and then the deformation value of the building appeared to accelerate. This demonstrates that the deformation process of mine subsidence can be reflected by the mine building construction.

5.2.3 Correlation Factor Analysis: From the Pearson correlation coefficient diagram (Figure 5), it can be observed that the surface deformation is triggered by multiple influencing factors. Among the factors related to deformation, the correlation coefficients are listed from high to low by taking their absolute values as follows: slope: 0.85; production scale per unit area: 0.59; mine elevation: -0.54; thickness of coal: -0.52; elevation: 0.50; land cover: -0.31; stratigraphic lithology: 0.23; aspect of slope: 0.17; coal bed pitch: -0.04; population density: 0.05; building height: 0.028. The two factors that have the greatest influence on deformation are the scale of production per unit area and slope.

5.3 Discussion

The original stress balance of the surrounding rock and soil will be disrupted after the underground coal seam is extracted, contributing to the rock layer deforming continuously or intermittently. The following points related to the application of InSAR technology to monitoring sedimentation can be discussed:

1) As for the application of InSAR in dense vegetation and low coherence regions, the Stacking technologies tend to amplify the effect of atmospheric errors for the interferograms with a short temporal baseline. The SBAS method obtains more accurate deformation due to the consideration of atmospheric delay. The majority of information of the IPTA results is missing in the mine area; thus, it is difficult to reflect the precise extent and boundary of the subsidence, although the deformation points at dense roads and buildings are well retained.

2) Surface settlement correlation variables in mining areas are multifaceted. In the correlation analysis section, the correlation between population density and ground deformation is very weak. The deformation is highly correlated with slope and population scale. Meanwhile, the aspect of slope is negatively correlated with the mine elevation, population density, and building height. The accuracy of these correlation results still needs to be studied with auxiliary materials.

6. Conclusion

In this research, we compared the application of three InSAR technologies in mining areas, obtained the time-series deformation of the Fengcheng mine region, and explored the correlation factors of ground surface sedimentation.

1) We studied the application of InSAR technologies (Stacking, SBAS, and IPTA) in mining by obtaining the annual deformation of the Fengcheng mine region. Firstly, four distinct sedimentation funnels were found in the mine area. Secondly, the IPTA, Stacking and SBAS methods obtained different deformation information because of the different process ways.

2) We obtained three-year long time series deformation of the four settlement centers with SBAS technique, and the profiles demonstrate that there were four main evolutionary processes, including the initial deformation stage, the steady deformation rate, the accelerated deformation stage, and the stable change stage.

3) Surface deformation is the generalized result of multiple factors. The natural factors were mainly affected by rainfall, and the human factors were mainly coal mining and construction of surface facilities. Furthermore, the three major categories of influencing factors, namely, topography and geomorphology, coal mining, and human activities, were selected and computed with the Grey correlation model, and it was concluded that two factors, the scale of production per unit area and the slope, have the greatest influence on the deformation.

4) The role of man-made factors is the most remarkable in Fengcheng mining area, mainly including mining and man-made structure construction; the former induced highly hazardous ground subsidence, and the latter’s deformation level is slow, usually needing a long period to accumulate to trigger the subsidence phenomena.

Declaration of Competing Interest

The authors declare that they have no known competing financial interests or personal relationships that could have appeared to influence the work reported in this paper.

Acknowledgments

We are grateful to USGS for providing the 1-arc-second SRTM DEM, ESA for providing Sentinel-1A/B data, and review experts for their suggestions and opinions. This research was supported by the Natural Science Foundation of China (42174055,42374040), the Research Fund for the Doctoral Program of East China University of Technology (No. DHBK2019187), the Science and Technology Research Project of Jiangxi Provincial Department of Education in 2021 (GJJ210722), the Key Laboratory for Digital Land and Resources of Jiangxi Province, East China University of Technology (DLLJ202105), and the Open Fund of Key Laboratory of Mine Environmental Monitoring and Improving around Poyang Lake, Ministry of Natural Resources (Grant No. MEMM1-2021-2022-23).

References

Amedeo, C., Gianmarco, B., Filippo, L., Francesca, D.P., 2023: Application of Multi-Temporal InSAR (MT-InSAR) for Structural Monitoring: The Case Study of Scrovegni Chapel in Padova. *Procedia Structural Integrity* 44, 1578-1585.

Baek, J., Kim, S.W., Park, H.J., Jung, H.S., Kim, K.D., Kim, J.W., 2008: Analysis of Ground Subsidence in Coal Mining Area Using SAR Interferometry. *Geosciences Journal* 12, 277-284.

Bateson, L., Cigna, F., Boon, D., Sowter, A., 2015: The Application of the Intermittent SBAS (ISBAS) InSAR Method to the South Wales Coalfield, UK. *International Journal of Applied Earth Observation and Geoinformation* 34, 249-257.

Benesty, J., Chen, J., Huang, Y., Cohen, I., 2009: Pearson Correlation Coefficient. In: Noise Reduction in Speech Pro-Cessing. Springer Topics in Signal Processing. Springer, Berlin, Heidelberg.

Berardino, P., Fornaro, G., Lanari, R., Sansosti, E., 2002: A New Algorithm for Surface Deformation Monitoring Based on Small Baseline Differential SAR Interferograms. *IEEE Transactions on Geoscience and Remote Sensing* 40, 2375-2383.

Bhattacharya, A., Arora, M.K., Sharma, M.L., 2012: Usefulness of Synthetic Aperture Radar (SAR) Interferometry for Digital Elevation Model (DEM) Generation and Estimation of Land Surface Displacement in Jharia Coal Field Area. *Geocarto International* 27, 57 - 77.

Carnec, C., Massonnet, D., King, C., 1996: Two Examples of the Use of SAR Interferometry on Displacement Fields of Small Spatial Extent. *Geophysical Research Letters* 23, 3579-3582.

Casu, F., Manconi, A., Pepe, A., Lanari, R., 2011: Deformation Time-Series Generation in Areas Characterized by Large Displacement Dynamics: The SAR Amplitude Pixel-

Offset SBAS Technique. *IEEE Transactions on Geoscience and Remote Sensing* 49, 2752-2763.

Colesanti, C., Mouélic, S.L., Bennani, M., Raucoules, D., Carnec, C., Ferretti, A., 2005: Detection of Mining Related Ground Instabilities Using the Permanent Scatterers Technique—A Case Study in the East of France. *International Journal of Remote Sensing* 26, 201 - 207.

De, C.L., Zinno, I., Manunta, M., Lanari, R., Casu, F., 2017: Large Areas Surface Deformation Analysis through a Cloud Computing P-SBAS Approach for Massive Processing of DInSAR Time Series. *Remote Sensing of Environment* 202, 3-17.

Fan, H.D., Wang, L., Wen, B.F., Du, S., 2021: A New Model for Three-Dimensional Deformation Extraction with Single-Track InSAR Based on Mining Subsidence Characteristics. *International Journal of Applied Earth Observation and Geoinformation* 94.

Ferretti, A., Fumagalli, A., Novali, F., Prati, C., Rocca, F., Rucci, A., 2011: A New Algorithm for Processing Interferometric Data-Stacks: SqueeSAR. *IEEE Transactions on Geoscience and Remote Sensing* 49, 3460-3470.

Ferretti, A., Prati, C.M., Rocca, F., 1999: Permanent Scatterers in SAR Interferometry. *IEEE 1999 International Geoscience and Remote Sensing Symposium*. IGARSS'99 (Cat. No.99CH36293) 3, 1528-1530 vol.3.

Fu, L., Wang, L., Han, J., 2013: Multivariable Forecasting Model Based on Trend Grey Correlation Degree and Its Ap-Plication. In: Qi, E., Shen, J., Dou, R. (Eds) the 19th International Conference on Industrial Engineering and Engi-Neering Management. . Springer, Berlin, Heidelberg.

Ge, L.L., Chang, H.C., Rizos, C., 2007: Mine Subsidence Monitoring Using Multi-Source Satellite SAR Images. *Photogrammetric Engineering and Remote Sensing* 73, 259-266.

Fengcheng City People's Government. 2020: Fengcheng Urban and Rural Master Plan and "Multi-Planning Integration" (2015-2030) http://www.jxfc.gov.cn/fcsrmzf/ghjh01/202306/0d4eb68fcf824266879883d20feb9f92.shtml.

Fengcheng City People's Government. 2022a: Mineral Resources Master Plan of Fengcheng City (2021-2025). http://www.jxfc.gov.cn/fcsrmzf/file/uploadfile/19/Attachment/a1eed0fcd3.pdf.

Fengcheng City People's Government. 2022b: Overall plan of land space of Fengcheng (2021-2035). http://www.jxfc.gov.cn/fcsrmzf/gsgg/202212/8f1af357211248359db59d4b985bffb6.shtml.

Graham, L.C., 1974: Synthetic Interferometer Radar for Topographic Mapping. *Proceedings of the IEEE* 62, 763-768.

Havazli, E., Wdowinski, S., 2021: Detection Threshold Estimates for InSAR Time Series: A Simulation of *Tropospheric Delay Approach. Sensors* 21.

Hooper, A., 2008: A Multi - Temporal InSAR Method Incorporating Both Persistent Scatterer and Small Baseline Approaches. *Geophysical Research Letters* 35.

Hu, B., 2012: Research on Karst Collapse and Destruction in Pinghu Coal Mine, Fengcheng Mining Area. *Mine Surverin*g, 1-4+21.

Jung, H.C., Kim, S.W., Jung, H.S., Min, K.D., Won, J.S., 2007: Satellite Observation of Coal Mining Subsidence by Persistent Scatterer Analysis. *Engineering Geology* 92, 1-13.

Karra, K., Kontgis, C., Zoe, S.W., Mazzariello, J.C., Mathis, M., Brumby, S.P., 2021. "Global Land Use / Land Cover with Sentinel 2 and Deep Learning." Paper presented at the 2021 *IEEE International Geoscience and Remote Sensing Symposium IGARSS*, 11-16 July 2021.

Liu, Z.G., Bian, Z.F., Lü, F.X., Dong, B.Q., 2013: Monitoring on Subsidence Due to Repeated Excavation with DInSAR Technology. *International Journal of Mining Science and Technology* 23, 173-178.

Ng, A.H.M., Ge, L.L., Du, Z.Y., Wang, S.R., Ma, C., 2017: Satellite Radar Interferometry for Monitoring Subsidence Induced by Longwall Mining Activity Using Radarsat-2, Sentinel-1 and Alos-2 Data. *International Journal of Applied Earth Observation and Geoinformation* 61, 92-103.

Ng, A.H.M., Ge, L.L., Zhang, K., Chang, H.C., Li, X.J., Rizos, C., Omura, M., 2011: Deformation Mapping in Three Dimensions for Underground Mining Using InSAR – Southern Highland Coalfield in New South Wales, Australia. *International Journal of Remote Sensing* 32, 7227-7256.

Osmanoglu, B., Sunar, F., Wdowinski, S., Cabral-Cano, E., 2016: Time Series Analysis of InSAR Data: Methods and Trends. *ISPRS Journal of Photogrammetry and Remote Sensing* 115, 90-102.

Perski, Z., 1998: Applicability of ERS-1 and ERS-2 InSAR for Land Subsidence Monitoring in the Silesian Coal Mining Region, Poland.

Przyłucka, M., Herrera, G., Graniczny, M., Colombo, D., Béjar-Pizarro, M., 2015: Combination of Conventional and Advanced DInSAR to Monitor Very Fast Mining Subsidence with Terrasar-X Data: Bytom City (Poland). *Remote Sensing* 7, 5300-5328.

Sandwell, D.T., Price, E.J., 1998: Phase Gradient Approach to Stacking Interferograms. *Journal of Geophysical Research: Solid Earth* 103, 30183-30204.

Wang, L., Deng, K., Zheng, M., 2020: Research on Ground Deformation Monitoring Method in Mining Areas Using the Probability Integral Model Fusion D-InSAR, Sub-Band InSAR and Offset-Tracking. *International Journal of Applied Earth Observation and Geoinformation* 85, 101981.

Wang, L., Teng, C.Q., Jiang, K.G., Jiang, C., Zhu, S.J., 2022: D-InSAR Monitoring Method of Mining Subsidence Based on Boltzmann and Its Application in Building Mining Damage Assessment. *KSCE Journal of Civil Engineering* 26, 353-370.

Wang, R., 2022: Research on Multi-Source Data Fusion Technology and Application for Mining Subsidence Monitoring. Doctoral Degree, China University of Mining and Technology.

Wang, X.Y., Yang, Y.M., Xia, Y.P., Chen, S.Q., She, Y.L., 2023: Integrating SAR and Geographic Information Data Revealing Land Subsidence and Geological Risks of Shanghai City. *Applied Sciences* 13.

Wang, X.Y., Zhang, Q., Zhao, C.Y., Qu, F.F., Zhang, J.Q., 2018: A Novel Method of Generating Deformation Time-Series Using Interferometric Synthetic Aperture Radar and Its Application in Mexico City. *Remote Sensing* 10.

Wegmuller, U., Strozzi, T., Werner, C., Wiesmann, A., Benecke, N., Spreckels, V., 2000: Monitoring of Mining-Induced Surface Deformation in the Ruhrgebiet (Germany) with SAR Interferometry. *IEEE 2000 International Geoscience and Remote Sensing Symposium. Proceedings* (Cat. No.00CH37120), 24-28.

Werner, C., Wegmuller, U., Strozzi, T., Wiesmann, A., 2003: Interferometric Point Target Analysis for Deformation Mapping. *IEEE International Geoscience and Remote Sensing Symposium. Proceedings* (IEEE Cat. No.03CH37477), 21-25.

Wu, W.B., Ma, J., Banzhaf, E., Meadows, M.E., Yu, Z.W., Guo, F.X., Sengupta, D., Cai, X.X., Zhao, B., 2023: A First Chinese Building Height Estimate at 10 m Resolution (Cnbh-10 m)

Using Multi-Source Earth Observations and Machine Learning. *Remote Sensing of Environment* 291, 113578.

Xu, Y.Z., Li, T., Tang, X.M., Zhang, X., Fan, H D., Wang, Y.W., 2022: Research on the Applicability of DInSAR, Stacking-InSAR and SBAS-InSAR for Mining Region Subsidence Detection in the Datong Coalfield. *Remote Sensing* 14, 3314.

Yao, S., He, Y., Zhang, L.F., Yang, W., Chen, Y., Sun, Q., Zhao, Z.A., Cao, S.P., 2023: A Convlstm Neural Network Model for Spatiotemporal Prediction of Mining Area Surface Deformation Based on SBAS-InSAR Monitoring Data. *IEEE Transactions on Geoscience and Remote Sensing* 61.

Yuan, M.Z., Li, M., Liu, H., Lv , P.Y., Li, B., Zheng, W.B., 2021: Subsidence Monitoring Base on SBAS-InSAR and Slope Stability Analysis Method for Damage Analysis in Mountainous Mining Subsidence Regions. *Remote Sensing* 13.

Zhang, B., Li, J.Y., Ren, H.R., 2019: Using Phase Unwrapping Methods to Apply D-InSAR in Mining Areas. *Canadian Journal of Remote Sensing* 45, 1-9.

Zhang, L., Lu, Z., Ding, X., Jung, H.A., Feng, G., Lee, C.W., 2012: Mapping Ground Surface Deformation Using Temporarily Coherent Point SAR Interferometry: Application to Los Angeles Basin. *Remote Sensing of Environment* 117, 429-439.

Zheng, M.N., Deng, K.Z., Fan, H.D., Du, S., 2018: Monitoring and Analysis of Surface Deformation in Mining Area Based on InSAR and Grace. *Remote Sensing* 10.

Zhou, D.W., Qi, L.Z., Zhang, D.M., Zhou, B.H., Guo, L.L., 2020: Unmanned Aerial Vehicle (UAV) Photogrammetry Technology for Dynamic Mining Subsidence Monitoring and Parameter Inversion: A Case Study in China. *IEEE Access* 8, 16372-16386.